Nanoscale

PAPER

View Article Online
View Journal | View Issue

Cite this: *Nanoscale*, 2014, **6**, 14911

Atomistic mechanisms of codoping-induced p- to n-type conversion in nitrogen-doped graphene†

Hyo Seok Kim, Han Seul Kim, Seong Sik Kim and Yong-Hoon Kim*

Received 29th August 2014,
Accepted 8th October 2014

DOI: 10.1039/c4nr05024j

www.rsc.org/nanoscale

It was recently shown that nitrogen-doped graphene (NG) can exhibit both p- and n-type characters depending on the C–N bonding nature, which represents a significant bottleneck for the development of graphene-based electronics. Based on first-principles calculations, we herein scrutinize the correlations between the atomic and electronic structures of NG and particularly explore the feasibility of converting p-type NG with pyridinic, pyrrolic, and nitrilic N atoms into n- or bipolar type by introducing an additional dopant atom. Of the nine candidates B, C, O, F, Al, Si, P, S, and Cl, we find that B-, Al-, and P-codoping can anneal even relatively large vacancy defects in p-type NG. It will be also shown that, while the NG with pyridinic N can be converted into the n-type *via* codoping, only a bipolar type conversion can be achieved for the NG with nitrilic or pyrrolic N. The amount of work function reduction was up to 0.64 eV for the pyridinic N next to a monovacancy. The atomistic origin of such diverse type changes is analyzed based on Mulliken and crystal orbital Hamiltonian populations, which provide us with a framework to connect the local bonding chemistry with the macroscopic electronic structure in doped and/or defective graphene. Moreover, we demonstrate that the proposed codoping scheme can recover the excellent charge transport properties of pristine graphene. Both the electronic type conversion and conductance recovery in codoped NG should have significant implications for the electronic and energy device applications.

1. Introduction

Because of its unique structural, electronic, and transport properties,[1–4] graphene is regarded as one of the best candidate materials to be incorporated into the next-generation electronic, energy, and biodevices.[5–7] To realize its potential for device applications, reliable methods to tailor the atomic and electronic structures of graphene are required.[8–10] Doping of graphene has been extensively investigated in this context, and among various options, nitrogen doping has emerged as one of the most effective schemes to improve the diverse functionalities of graphene[10–20] and especially to achieve n-type doping that is crucial for electronic applications.[21–25] Unfortunately, recent experimental and theoretical studies have revealed that N-doped graphene (NG) can assume both n- and p-type characters depending on the bonding nature of N atoms, namely, n-type for graphitic N and p-type for pyridinic, pyrrolic, and nitrilic N.[25–27] The question then arises as to how one can achieve robust n-type NG, and at the more fundamental level, which factors determine the structure–property relationships of NG. The latter should have significant implications for practical applications. For example, the bonding state of the N atom was found to critically affect the oxygen reduction reaction (ORR) activity in fuel cell cathodes, but the nature of the catalytically active sites remains controversial.[15,17]

Carrying out first-principles density functional theory (DFT) and DFT-based non-equilibrium Green's function (NEGF) calculations, we herein systematically investigate the atomistic origins of p-type character in NG with pyridinic, pyrrolic, and nitrilic N and the feasibility of achieving robust n-type graphene by incorporating a codopant atom. Graphene codoped with N and B or N and P has already been synthesized and shown to improve the ORR performance,[28,29] but the atomistic details and mechanism of the synergistic effects associated with B, N- and P, N-codoping have not yet been understood. We first consider the energetic feasibility of introducing an additional atom into various p-type NG defect sites and show that B, Al, Si and P atoms can structurally anneal even relatively large vacancy defects next to the pyridinic, nitrilic, and pyrrolic N atoms. We find that, except for Si, the B, Al, and P codoping can convert the pyridinic NG into n-type and the nitrilic and pyrrolic NG into bipolar type, and thus effectively eliminate the p-type character of NG. Based on the Mulliken

Graduate School of Energy, Environment, Water, and Sustainability, Korea Advanced Institute of Science and Technology, 291 Daehak-ro, Yuseong-gu, Daejeon 305-701, Korea. E-mail: y.h.kim@kaist.ac.kr; Fax: +82-42-350-1710; Tel: +82-42-350-1717

† Electronic supplementary information (ESI) available: Relative formation energies for the codoping of V_1-N^{py}_{1-2} and V_2-N^{py}_{1-3}; atomic structures and DOS of F + V_1-N^{py}_3 and F + V_2-N^{py}_4; atomic structures, DOS, and COHP of the B/Al/Si/P-codoped V_1-N^{py}_{1-2} and V_2-N^{py}_{1-3}; decomposed COHPs of B/Al/Si/P + V_1-N^{py}_3, B/Al/Si/P + V_2-N^{py}_4, B + N^{nit}, and Si + N^{nit}. See DOI: 10.1039/C4NR05024J

and crystal overlap Hamilton population (COHP) analyses, we further establish the basis to understand how the macroscopic electronic type change in NG is induced from the atomistic bonding viewpoint. Finally, we will demonstrate that an additional benefit of the codoping approach is the recovery of an excellent charge transport capacity of pristine graphene, in line with the recovery of the sp^2 bonding network upon the healing of vacancy defects.

2. Calculation methods

We performed spin-polarized DFT calculations within the Perdew–Burke–Ernzerhof parameterization of generalized gradient approximation[30] using the SIESTA software.[31] The atomic cores were replaced by the Troullier–Martins-type norm-conserving pseudopotentials,[32] and the double-ζ-plus-polarization level numerical atomic basis sets defined by the confinement energy of 80 meV were adopted. For the supercell of 9 × 9 graphene unit cells (see ESI Fig. S1†), we used a mesh cut-off energy of 200 Ry and the 3 × 3 × 1 $\vec{k}$-point sampling in the Monkhorst–Pack scheme.[33] A finer 30 × 30 × 1 $\vec{k}$-point mesh was sampled for the calculation of density of states (DOS) and COHP. The vacuum region of the supercell in the direction perpendicular to the graphene plane was set to 25 Å. We have calculated the work function Φ using the equation:

$$\Phi = V_{\mathrm{vac}} - E_{\mathrm{F}}, \quad (1)$$

where E_{F} is the Fermi energy and V_{vac} is the macroscopic average potential in the vacuum, defined as the midpoint between the graphene layer and its neighboring images.[34] The doping charge density was calculated according to

$$n = \frac{(E_{\mathrm{D}} - E_{\mathrm{F}})^2}{\pi(\hbar v_{\mathrm{F}})^2}, \quad (2)$$

where E_{D} is the Dirac point energy and v_{F} is the Fermi velocity, 1×10^6 m s^{-1}.[3,34]

Transmission functions $T(E)$ were calculated using the DFT-based NEGF method,[35] as implemented in TranSIESTA.[36] We used the periodic cell composed of six dimer lines in the transport normal direction (14.80 Å) and sampled 66 $\vec{k}_{\perp}$ points. In the transport direction, we used eight and two zigzag chains to model the channel and electrode regions, respectively, and the surface Green's functions were obtained for the corresponding electrode models sampled with the 25 $\vec{k}_{||}$ points (see ESI Fig. S1†). For calculating $T(E)$, the energy was scanned from −1.0 eV to 1.0 eV with respect to E_{F} with the 0.001 eV resolution. In many cases, we have crosschecked the validity of our results using SeqQuest and our in-house NEGF code.[37,38]

3. Results and discussion

In this work, in addition to graphitic N (N^{gr}, Fig. 1a), we considered four other representative NG conformations: pyridinic N next to a monovacancy (V_1-N^{py}, Fig. 1b) and a divacancy (V_2-N^{py}, Fig. 1c), nitrilic N next to a divacancy (N^{nit}, Fig. 1d), and pyrrolic N next to a trivacancy (N^{pyrr}, Fig. 1e).[25,39,40] Recent experimental and theoretical reports showed that, despite the high formation energies, vacancy defects can form within the graphene sheets by, *e.g.*, ion or electron irradiation.[41] In the presence of vacancy defects, the pyridinic N configurations were shown to become energetically more favorable than the graphitic N one.[26,42]

In Table 1, we show the zero-temperature formation energies of the V_1-N^{py}, V_2-N^{py}, N^{nit}, and N^{pyrr} structures calculated according to

$$E_{\mathrm{f}}(\mathrm{NG}) = (E_{\text{N-doped}} + x\mu_{\mathrm{C}}) - (E_{\text{pristine}} + y\mu_{\mathrm{N}} + z\mu_{\mathrm{H}}), \quad (3)$$

where $E_{\text{N-doped/pristine}}$ are the total energies of N-doped/pristine graphenes, $\mu_{\mathrm{C/N/H}}$ are the chemical potentials (total energies per atom in their elemental reference phases) of C/N/H, x is the number of C atoms removed from the graphene sheet during the vacancy formation, y is the number of N atoms, and z is the number of H atoms (2 for N^{nit} and 0 otherwise). The chemical potentials of C, N, and H were extracted from graphene, the N_2 molecule, and the H_2 molecule, respectively. Note that we included two pyridinic conformations, because the V_2-N^{py} configuration is energetically even more favorable than the N^{nit} and N^{pyrr} counterparts. For the V_1-N^{py} and V_2-N^{py} cases, we additionally considered the substitution of different numbers of N atoms around the vacancy sites, V_1-N^{py}_{α} (α = 1–3) and V_2-N^{py}_{β} (β = 1–4), and found that the maximum concentration of pyridinic N atoms around the mono- and divacancies (trimerized V_1-N^{py}_3, tetramerized pyridine-like V_2-N^{py}_4, respectively) is energetically preferred (Table 1).[26]

An important objective of the present work is to provide an atomistic understanding of the nitrogen bonding nature in NG and its modification upon codoping. For this purpose, we will demonstrate that the combination of band structure, DOS, Mulliken population, and COHP[43] provides systematic and detailed information that guides the route toward the desired n-type or bipolar conversion. The COHP is defined by the DOS multiplied by the Hamiltonian of the corresponding element, and the negative COHP values (–COHP) give positive and negative signs for the bonding and antibonding states, respectively. The DOS, COHP normalized by the number of bonds and the band structure data of N^{gr}, V_1-N^{py}_3, V_2-N^{py}_4, N^{nit}, and N^{pyrr} are shown in Fig. 1, and their electronic structures are summarized in Table 2.

The doping type of graphitic NG is n-type, *i.e.*, E_{D} is located below E_{F} (Fig. 1a, middle and bottom panels). This results from the electron transfer from the N^{gr} atoms to the π^* states of graphene. Visualizing the Mulliken charge populations as in Fig. 2a, we can observe that the electrons donated from N^{gr} are distributed throughout the graphene basal plane or become mobile charges. The amount of donated charges extracted from the population analysis is 0.402 electron per nitrogen atom, which is in excellent agreement with the experimental estimation.[44] It results in the upward shift of E_{F} from E_{D} of the pristine graphene case to the graphene conduction band or the lowering of the work function by 0.37 eV. The calculated

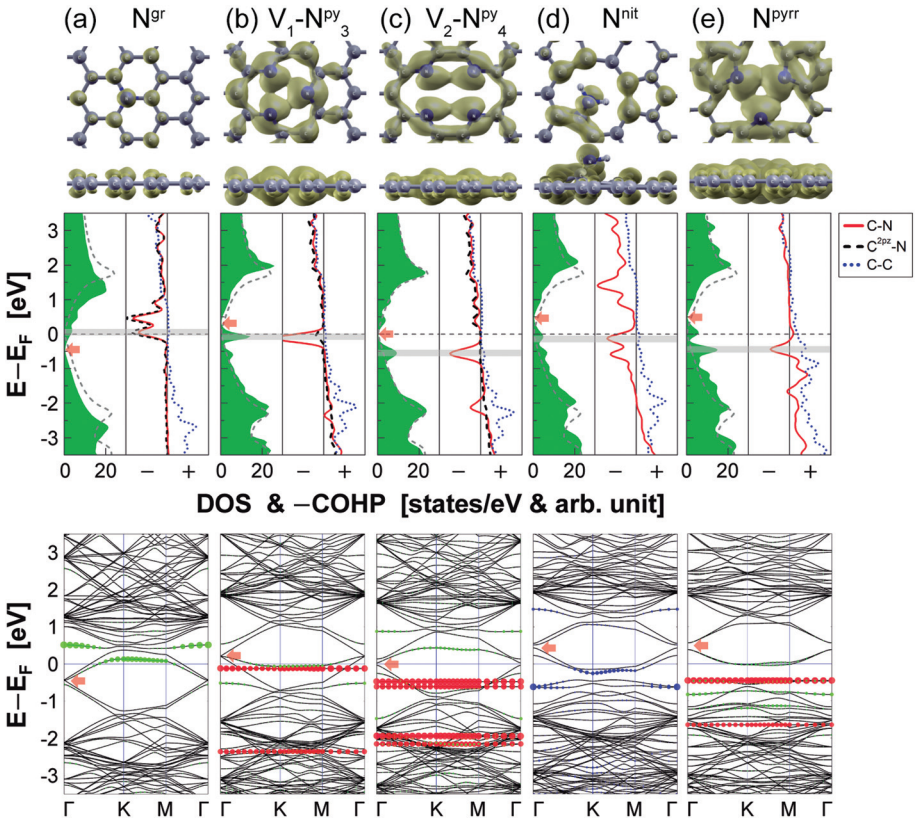

Fig. 1 Atomic structures (top panels), DOS (middle left panels), COHPs (middle right panels), and band structures (bottom panels) of (a) N^{gr}, (b) V_1-N_3^{py}, (c) V_2-N_4^{py}, (d) N^{nit}, and (e) N^{pyrr}. On the top of the atomic structures, we overlay the LDOS for the energy ranges marked by shaded regions in the DOS/COHP plots at the isovalues of 5×10^{-4} e Å^{-3}. In the DOS plots, pristine graphene DOS are shown together (gray dashed lines), and the Dirac points are marked by red arrows. In the COHP plots, we show the C–C (blue dotted lines) and C–N (red solid lines) bond curves and additionally the C $2p_z$ orbitals–N bond data (black dashed lines) for V_1-N_3^{py} and V_2-N_4^{py}. In the bandstructures, green, red, and blue dots represent the projection of N π states, N σ states, and N atoms, respectively. The weight is represented by dot size.

Table 1 The formation energies of various N doped graphene models considered in this work

	Formation energy [eV]			
Number of N atoms	V_1-N^{py}	V_2-N^{py}	N^{nit}	N^{pyrr}
1	5.14	7.44	7.66	—
2	4.48	5.53	—	—
3	2.76	4.77	—	9.06
4	—	2.90	—	—

charge-carrier density of 11.31×10^{12} cm^{-2} for our model with an N atom doping ratio of 0.62% N atoms per C atom (N atom density of 2.31×10^{13} cm^{-2}) is in good agreement with the experimental estimate of 5.42×10^{12} electrons per cm^2 for the 0.34% N atoms per C atom doping. The COHP curve shows that these impurity resonant states have antibonding characters, being identified as the strong negative COHP peaks right above E_F (thus E_D). The energetic locations of the antibonding COHP peaks are E_F + 0.07 eV and E_F + 0.45 eV. These peak locations depend on the supercell size, or the doping ratio, and are expected to converge to an experimentally observed single peak at about E_F + 0.14 eV.[27,45]

On the other hand, the electronic structures of the other three V_1-N_3^{py}, N^{nit}, and N^{pyrr} NG are p-type or E_F has been shifted downward into the valence bands (Fig. 1b, d and e, middle and bottom panels). This should mainly result from the presence of vacancy defect states (whose LDOS are shown in Fig. 1b, d and e, top panels), which behave as acceptor states with missing π-electrons.[24,25,27] Note that in these cases the impurity states appear in the COHP plots as strong antibonding peaks right below E_F (thus E_D). Interestingly, the V_2-N_4^{py} case shows a bipolar character (E_D nearly coincides with E_F).[27] To understand such discrepancies, we analyzed the Mulliken populations as shown in Fig. 2b–d for V_1-N_3^{py}, V_2-N_4^{py} and N^{pyrr}, respectively (the N^{nit} diagram is similar to N^{pyrr} and is not shown). They show that the spatial range of charge redistribution around the nitrogen-vacancy complexes discriminates the V_1-N_3^{py} and N^{pyrr} cases from the V_2-N_4^{py} counterpart: we observed the depletion of electrons throughout the entire graphene basal plane in the former, but rather localized charge depletion around the nitrogen-vacancy site in the latter (compare Fig. 2c with Fig. 2b and d). Related with these charge transfer characters, the impurity states strongly hybridize with the carbon $2p_z$ orbitals or graphene π states (existence of an antibonding C $2p_z$–N COHP peak) in V_1-N_3^{py} (Fig. 1b, COHP

Table 2 The C–N bond lengths, work functions, doping types, and doping concentrations of different NG configurations and their codoped cases. For pristine graphene, the C–C bond length is given. For B + V_2-N_4^{py}, two C–N bond lengths (for the B-attached and non-B-attached sides, see Fig. 4e) are given

Structure	l_{C-N} [Å]	Φ [eV]	Doping type	n [10^{12} cm^{-2}]
Pristine	1.43	4.23	—	—
N^{gr}	1.42	3.86	n	11.31
V_1-N_3^{py}	1.35	4.48	p	−9.31
B + V_1-N_3^{py}	1.41	3.84	n	16.03
Al + V_1-N_3^{py}	1.38	3.86	n	15.57
Si + V_1-N_3^{py}	1.38	3.84	n	12.82
P + V_1-N_3^{py}	1.40	3.93	n	10.58
V_2-N_4^{py}	1.35	4.32	—	—
B + V_2-N_4^{py}	1.42/1.39	3.88	n	10.52
Al + V_2-N_4^{py}	1.40	3.80	n	9.80
Si + V_2-N_4^{py}	1.40	3.86	n	11.48
P + V_2-N_4^{py}	1.39	3.86	n	5.56
N^{nit}	1.35	4.53	p	−11.68
B + N^{nit}	1.46	4.13	—	—
Al + N^{nit}	1.49	4.13	—	—
Si + N^{nit}	1.47	4.34	p	−8.82
P + N^{nit}	1.47	4.11	—	—
N^{pyrr}	1.41	4.61	p	−19.36
B + N^{pyrr}	1.51	4.20	—	—
Al + N^{pyrr}	1.45	4.15	—	—
Si + N^{pyrr}	1.47	4.22	—	—
P + N^{pyrr}	1.48	4.21	—	—

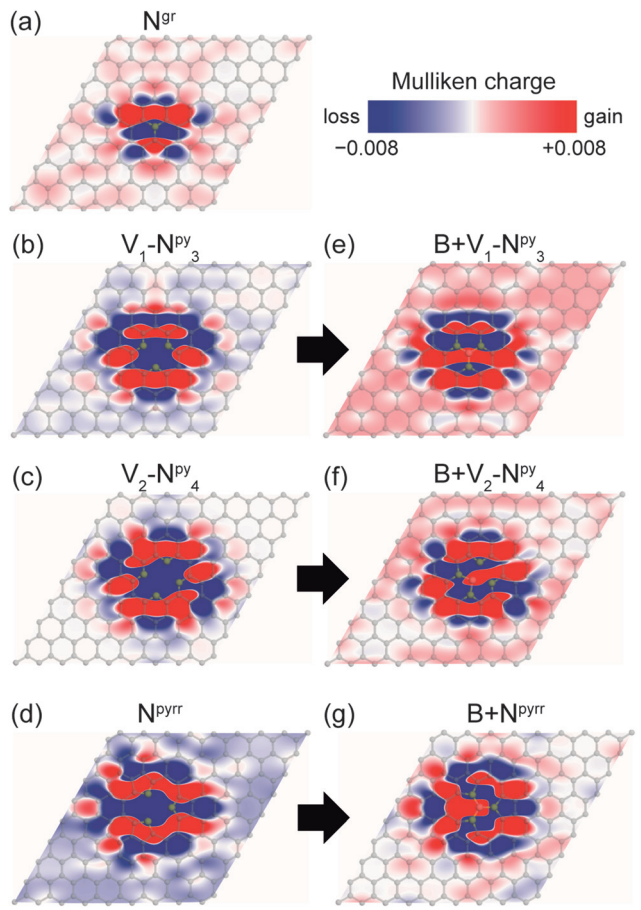

Fig. 2 Mulliken population analysis of (a) N^{gr}, (b)V_1-N_3^{py}, (c) V_2-N_4^{py}, (d) N^{pyrr}, (e) B + V_1-N_3^{py}, (f) B + V_2-N_4^{py}, and (g) B + N^{pyrr}. The blue and red colors represent the loss and gain of electrons, respectively.

panel, shaded region near E_F), whereas the hybridization is very weak (absence of an antibonding C $2p_z$–N COHP peak) in V_2-N_4^{py} (Fig. 1c, COHP panel, shaded region at $E - E_F \approx 0.5$ eV).

We now move on to consider the possibility of codoping the p-type NG. Since the presence of a vacancy defect is the precondition for the existence of V_1-N_3^{py}, V_2-N_4^{py}, N^{nit}, and N^{pyrr} sites, we focused on examining whether the vacancy defects can be healed by introducing a codopant. In addition to C, eight light elements, B, O, F, Al, Si, P, S, and Cl, were considered as codoping candidates. For the fully optimized structures X + V_1-N_{1-3}^{py}, X + V_2-N_{1-4}^{py}, X + N^{nit}, and X + N^{pyrr} (X = B, C, O, F, Al, Si, P, S, and Cl), we have calculated the formation energies,

$$E_f(\mathrm{X+NG}) = (E_{\mathrm{codoped}} + x\mu_C) - (E_{\mathrm{pristine}} + y\mu_N + z\mu_H + \mu_X), \quad (4)$$

where $E_{codoped}$ is the total energy of codoped NG, $\mu_{C/N/H/X}$ are the chemical potentials of C, N, H, and the codopant X, x/y are the numbers of removed/added C/N atoms with respect to the pristine graphene, and z is the number of added H atoms (2 for N^{nit} and 0 otherwise). The chemical potentials of B, O, F, Al, Si, P, S, and Cl were obtained from the α-rhombohedral boron, O_2 molecule, F_2 molecule, face-centered cubic aluminum, diamond cubic Si, black phosphorus, orthorhombic sulfur (α-S_8), and Cl_2 molecule, respectively. The formation energies relative to those of NG,

$$E_{rf}(\mathrm{X+NG}) = E_f\ (\mathrm{X+NG}) - E_f\ (\mathrm{NG}), \quad (5)$$

which represent the energetic feasibility of annealing the vacancy defects of p- or bipolar-type NG by the codoping approach, are summarized in Fig. 3 (for V_1-N_{1-3}^{py} and V_2-N_{1-4}^{py},

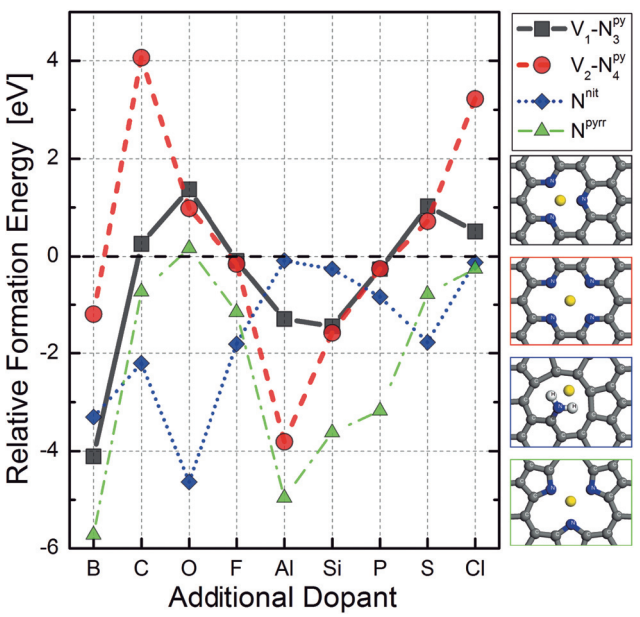

Fig. 3 Relative formation energies of introducing an additional dopant atom into V_1-N_3^{py} (black squares), V_2-N_4^{py} (red circles), N^{nit} (blue diamonds), and N^{pyrr} (green triangles).

only the energetically most favorable V_1-N_3^{py} and V_2-N_4^{py} cases are shown. See ESI Fig. S2 and S3† for the other cases).

First, we find that, except for O + N^{pyrr}, both N^{nit} and N^{pyrr} defects can be annealed by all of the above codoping elements (negative E_{rf}), because the formation energies of N^{nit} and N^{pyrr} are rather large to begin with (Table 1) and their relatively large vacancies can easily accommodate an additional dopant atom. However, incorporating an additional dopant atom into the energetically more favorable pyridinic NG was found to be rather difficult: it was determined that the V_1-N_3^{py} and V_2-N_4^{py} defects can be annealed with only a B, F, Al, Si, or P atom. We found that the energetically less favorable pyridinic NG with lower N concentrations can also accommodate these elements (see ESI Fig. S2 and S3†). The results indicate that an N^{py} to N^{gr} conversion scheme solely based on the carbon source[24] will be limited in that di- or larger vacancies cannot be annealed. Although F codoping of p-type NG might be energetically feasible, it is found that the F atom cannot structurally passivate the vacancy defects in the V_1-N_3^{py} and V_2-N_4^{py} cases and accordingly the electronic structures of F + V_1-N_3^{py} and F + V_2-N_4^{py} still maintain the p-type and bipolar characters, respectively (see ESI Fig. S4†). This leaves B, Al, Si, and P as the codoping candidates for the n-type conversion of p-type NG.

We first focus on the pyridinic NG codoped with B, Al, Si, and P, whose fully relaxed geometries and electronic structures are shown in Fig. 4. The C–N bond lengths of pyridinic NG are elongated when the vacancy is annealed by the codopant (Table 2). We further found that the trend of energetic stability of codoped NG (Fig. 3) is strongly related with the planarity of their geometries. For example, B can anneal the V_1-N_3^{py} defect without protrusion (Fig. 4a), which makes its E_{rf} larger than those of Al, Si, and P. Similarly, Al can anneal the V_2-N_4^{py} defect in a fourfold-coordinated planar configuration (Fig. 4f), which makes it an energetically more favorable codopant than B, Si, and P.

In terms of electronic structures (Fig. 4, bottom panels, and Table 2), we find that all the X + V_1-N_3^{py} and X + V_2-N_4^{py} cases (X = B/Al/Si/P) become n-type, or E_D is now located below E_F.

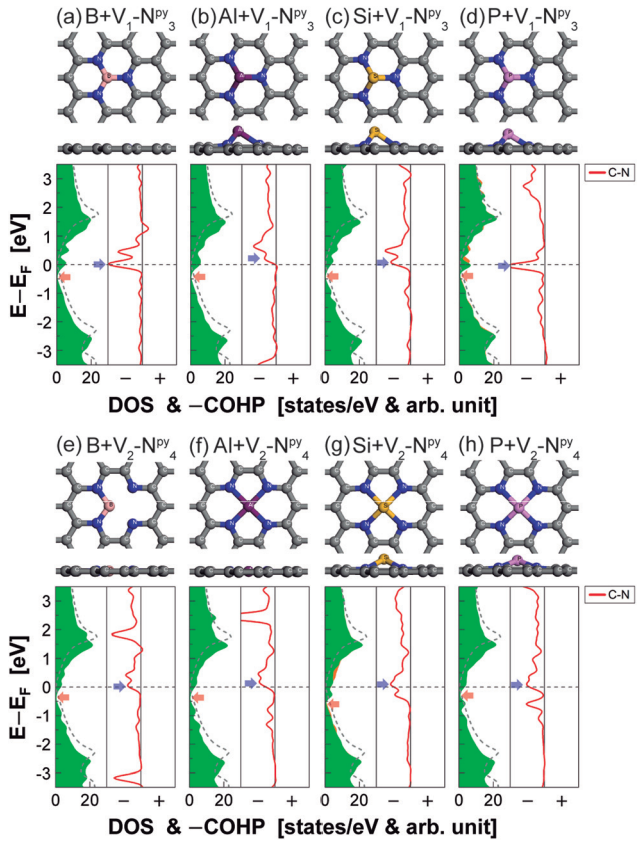

Fig. 4 Atomic structures (top panels), DOS (bottom left panels), and COHPs (bottom right panels) of (a) B + V_1-N_3^{py}, (b) Al + V_1-N_3^{py}, (c) Si + V_1-N_3^{py}, (d) P + V_1-N_3^{py}, (e) B + V_2-N_4^{py}, (f) Al + V_2-N_4^{py}, (g) Si + V_2-N_4^{py}, and (h) P + V_2-N_4^{py}. In the DOS plots, pristine graphene DOS are shown together (gray dashed lines), and the Dirac points are marked by red arrows. In the COHP plots, we show the C–N (red solid lines) bond data. For the slightly spin-polarized P + V_1-N_3^{py} and P + V_1-N_3^{py} cases, we show both the majority (green filled lines) and minority (orange filled lines) DOS.

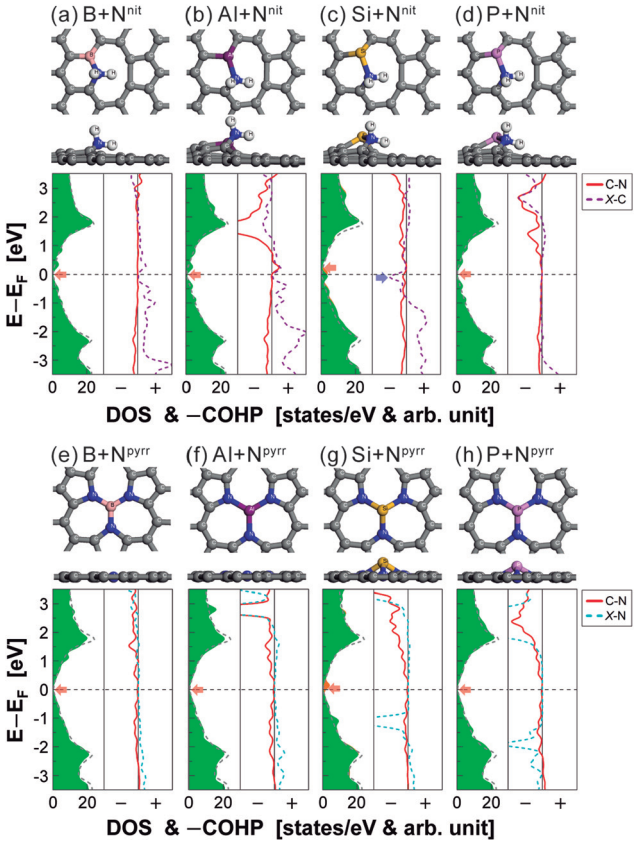

Fig. 5 Atomic structures (top panels), DOS (bottom left panels), and COHPs (bottom right panels) of (a) B + N^{nit}, (b) Al + N^{nit}, (c) Si + N^{nit}, (d) P + N^{nit}, (e) B + N^{pyrr}, (f) Al + N^{pyrr}, (g) Si + N^{pyrr}, and (h) P + N^{pyrr}. In the DOS plots, pristine graphene DOS are shown together (gray dashed lines), and the Dirac points are marked by red arrows. In the COHP plots, the C–N (red solid lines), X–C (purple dashed lines), and X–N (cyan dashed lines) bond curves are shown. For the slightly spin-polarized Si + N^{nit} and Si + N^{pyrr} cases, we show both the majority (green filled lines) and minority (orange filled lines) DOS.

The passivation of V_1-N_3^{py} and V_2-N_4^{py} vacancy defects by codoping of B/Al/Si/P allows the charge transfer from the N atoms to the graphene π^* states (Fig. 2e and f) as in the case of N^{gr} (Fig. 2a). The alteration of the electronic type change is also easily identified in the COHP data, in which we observe strong antibonding C–N peaks that are pinned near E_F or the downward shift of E_D below E_F. The reduction of work function for V_1-N_3^{py} and V_2-N_4^{py} was up to 0.62 eV and 0.52 eV upon codoping of B/Si and Al, respectively.

To further understand the microscopic mechanisms of electronic type conversion in X + V_1-N_3^{py} and X + V_2-N_4^{py}, we have decomposed the C–N COHPs into different orbital contributions (Fig. S5†) and found that the C–N antibonding COHP peaks mostly come from the C $2p_z$–N antibonds. Namely, the insertion of a B/Al/Si/P atom into V_1-N_3^{py} or V_2-N_4^{py} and the subsequent annealing of vacancy allows the N atoms to directly couple with the sp^2 C network and behave like graphitic N. Whereas the amount of downward shift of E_D tends to decrease with the lowering of N concentrations, we have confirmed that the B, Al, Si, and P codoping of V_1-N_{1-2}^{py} and V_2-N_{1-3}^{py} in general changes their electronic type to n- or at least bipolar ones (see ESI Fig. S6–S10†).

Compared with the pyridinic cases, the nitrilic and pyrrolic NG show a different type of conversion behavior and thus become interesting comparative systems (Fig. 5 and Table 2). The C–N bond lengths in nitrilic and pyrrolic NG are more elongated than those in the pyridinic counterparts. We also observe that, except for the case of Si + N^{nit} (Fig. 5c, bottom panels), all of them show the bipolar property (Table 2). The different behavior between the N^{py} family (can be converted to the n-type) and N^{nit} or N^{pyrr} (can be converted only to the bipolar-type) upon the introduction of a codoping element can be understood from their band structure plots. While the pyridinic defect states can energetically mix with the π states of graphene (Fig. 1b and c, bottom panels), the nitrilic and pyrrolic defect states are energetically located further away from E_F and cannot strongly hybridize with the graphene π states (Fig. 1d and e, bottom panels).

In spite of the difference, we can generally conclude that the p-type character of the structurally more distorted and energetically less probable N^{nit} and N^{pyrr} defects (Table 1) can be also eliminated by B, Al, and P codoping. The COHPs of C–N in these cases are nearly zero around E_D, or the N atoms in the codoped N^{nit} and N^{pyrr} do not affect the sp^2 carbon network. The nature of charge distribution in X + N^{nit} and X + N^{pyrr} can be again visualized in the Mulliken population analysis plot as shown for the representative B + N^{pyrr} case in Fig. 2g, which shows that the net induced charge is localized near the defect sites as in the (bipolar) V_2-N_4^{py} (Fig. 2c).

It remains to be explained why the Si-codoped N^{nit} maintains the p-type character (Fig. 5c, bottom panel). To understand its origin, we have additionally analyzed the COHPs of various bonds (see ESI Fig. S11†), and found that Si + N^{nit} can be discriminated from the B/Al/P + N^{nit} counterparts by a strong antibonding Si–C COHP peak that appears below E_D and is pinned near E_F (Fig. 5c, bottom panel). On the other hand, the B–C in B + N^{nit} has bonding character around E_F (Fig. 5a, bottom panel).

We finally demonstrate a very desirable feature of the codoping approach in terms of charge transport characteristics. We show in Fig. 6a and b the transmission functions of (codoped) NG for the representative cases of (B+)V_1-N_1^{py} and

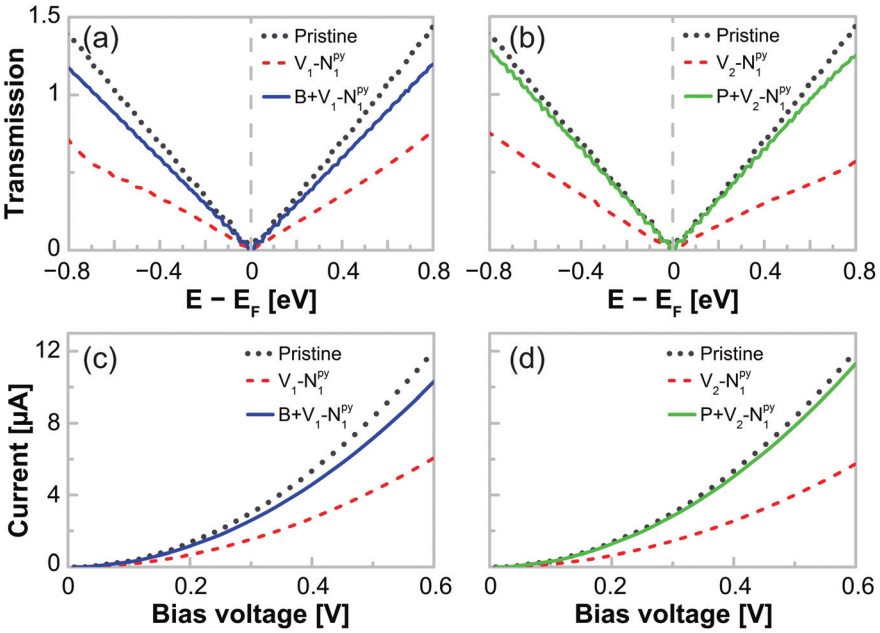

Fig. 6 Transmission functions of (a) V_1-N_1^{py} (red dashed line) and B + V_1-N_1^{py} (blue solid line) and (b) V_2-N_1^{py} (red dashed line) and P + V_2-N_1^{py} (green solid line). Current–bias voltage curves of (c) V_1-N_1^{py} (red dashed line) and B + V_1-N_1^{py} (blue solid line) and (d) V_2-N_1^{py} (red dashed line) and P + V_2-N_1^{py} (green solid line). As references, the pristine graphene transmission and current–bias voltage curves are shown together (gray dotted lines).

(P+)V_2-N_1^{py}. Note that in these NEGF calculations, unlike the DFT results that have been discussed so far, we are considering isolated doping sites sandwiched by two semi-infinite pristine graphene electrodes (see ESI Fig. S1†). The work function of the entire junction system is thus determined by the pristine graphene region, which results in the Dirac point located at E_F. The corresponding current–bias voltage curves calculated according to the Landauer–Büttiker formula,

$$I(V) = \frac{2e}{h}\int_{\mu_1}^{\mu_2} \mathrm{d}E\, T(E)[f(E-\mu_1) - f(E-\mu_2)], \qquad (6)$$

where $\mu_1 = E_F - 0.5$ eV and $\mu_2 = E_F + 0.5$ eV are shown together in Fig. 6c and d, respectively. For the untreated p-type NG models (V_1-N_1^{py} and V_2-N_4^{py}), we find that the localized defect states around vacancy sites result in currents much decreased compared with those of pristine graphene. However, upon introducing codopant atoms and healing the vacancy defects (B + V_1-N_1^{py} and P + V_2-N_1^{py}), we almost completely recover the currents of pristine graphene. We have recently obtained a similar behavior for B–N edge-doped graphene nanoribbons.[46]

The availability of a simple yet effective method to convert NG with mixed n- and p-type characters into near-uniform n-type NG will improve the performance and reliability of various graphene-based electronic devices such as all-graphene p–n junctions, field-effect transistors, integrated circuits, *etc.*[47–50] We additionally note that the codoping-induced type change in NG may have significant implications for energy applications.[10–20] In an effort to identify the catalytically active sites in NG with a significantly improved ORR performance, it was recently shown that the ORR activity in NG-based fuel cell cathodes is proportional to the graphitic N content.[17] On the other hand, it was experimentally demonstrated that the codoping of B or P into NG improves the ORR performance.[28,29] While the precise origin of the enhanced ORR activity in NG and codoped NG is not yet clear, we can propose that the codoping-induced conversion of mixed-type NG into uniformly n-type NG (*i.e.* generating more "effectively" graphitic N atoms) and the enhanced charge transport capacity will play an important role in enhancing the ORR activity.

4. Conclusion

In summary, based on fully first-principles computations, we have predicted that the post-synthetic codoping of p-type NG with B, Al, and P can anneal even relatively large vacancy defects associated with pyridinic, pyrrolic, and nitrilic N. We also found that, while the pyridinic NG can be converted into the n-type, only a bipolar type conversion is allowed for the nitrilic and pyrrolic counterparts. More importantly, employing novel analysis schemes, we have revealed the origin of p-type or bipolar behavior of NG and shown that the codoping and consequent healing of vacancy defects strongly modify the C–N antibonding character, its energetic position, and the spatial distribution of electrons donated from N atoms. We expect that this will provide in the future a framework to systematically characterize doped and/or defective graphene. Furthermore, we demonstrated that the codoping of p-type NG can recover the excellent charge transport capacity of pristine graphene, and suggested that together with the electronic type change it should have significant implications for energy and electronic device applications. In view of the experimental advances already made in the control of doping characters of NG,[15,17] we envisage that the facile post-synthetic codoping scheme proposed here will lead to new pathways for tailoring and enhancing the properties of graphene at the atomic level.

Note added in proof: After the submission of this work for publication, we became aware of ref. 51, in which the authors experimentally synthesized P, N-codoped graphene by a chemical vapor deposition method and found much improved air-stable n-type characteristics. In addition, in ref. 52, the authors theoretically predicted that dissociative adsorption of H_2 molecules on the trimerized and tetramerized pyridine-type defects is energetically favorable, and the adsorption of two H atoms changes their electronic properties from p-type to n-type doping.

Acknowledgements

This research was supported mainly by the Global Frontier Program (2013M3A6B1078881) and additionally by a Basic Science Research Grant (no. 2012R1A1A2044793), the Nano Material Technology Development Program (no. 2012M3A7B4049888), and the EDISON Program (no. 2012M3C1A6035684) of the National Research Foundation funded by the Ministry of Education Science and Technology of Korea. Computational resources were provided by the KISTI Supercomputing Center (no. KSC-2013-C3-046).

References

1 A. K. Geim and K. S. Novoselov, *Nat. Mater.*, 2007, **6**, 183.
2 A. H. C. Neto, F. Guinea, N. M. R. Peres, K. S. Novoselov and A. K. Geim, *Rev. Mod. Phys.*, 2009, **81**, 109–162.
3 N. M. R. Peres, *Rev. Mod. Phys.*, 2010, **82**, 2673–2700.
4 S. D. Sarma, S. Adam, E. H. Hwang and E. Rossi, *Rev. Mod. Phys.*, 2011, **83**, 407–470.
5 K. Kim, J.-Y. Choi, T. Kim, S.-H. Cho and H.-J. Chung, *Nature*, 2011, **479**, 338.
6 K. S. Novoselov, V. I. Falko, L. Colombo, P. R. Gellert, M. G. Schwab and K. Kim, *Nature*, 2012, **490**, 192.
7 J. Liu, Y. H. Xue, M. Zhang and L. M. Dai, *MRS Bull.*, 2012, **37**, 1265.
8 H. Liu, Y. Liu and D. Zhu, *J. Mater. Chem.*, 2011, **21**, 3335.
9 S. T. Pantelides, Y. Puzyrev, L. Tsetseris and B. Wang, *MRS Bull.*, 2012, **37**, 1187.
10 U. N. Maiti, W. J. Lee, J. M. Lee, Y. Oh, J. Y. Kim, J. E. Kim, J. Shim, T. H. Han and S. O. Kim, *Adv. Mater.*, 2014, **26**, 40.
11 Y. Wang, Y. Shao, D. W. Matson, J. Li and Y. Lin, *ACS Nano*, 2010, **4**, 1790.

12 L. Qu, Y. Liu, J.-B. Baek and L. Dai, *ACS Nano*, 2010, **4**, 1321.
13 A. L. M. Reddy, A. Srivastava, S. R. Gowda, H. Gullapalli, M. Dubey and P. M. Ajayan, *ACS Nano*, 2010, **4**, 6337.
14 H. Wang, C. Zhang, Z. Liu, L. Wang, P. Han, H. Xu, K. Zhang, S. Dong, J. Yao and G. Cui, *J. Mater. Chem.*, 2011, **21**, 5430.
15 Z. Luo, S. Lim, Z. Tian, J. Shang, L. Lai, B. MacDonald, C. Fu, Z. Shen, T. Yu and J. Lin, *J. Mater. Chem.*, 2011, **21**, 8038.
16 H. M. Jeong, J. W. Lee, W. H. Shin, Y. J. Choi, H. J. Shin, J. K. Kang and J. W. Choi, *Nano Lett.*, 2011, **11**, 2472.
17 L. Lai, J. R. Potts, D. Zhan, L. Wang, C. K. Poh, C. Tang, H. Gong, Z. Shen, J. Lin and R. S. Ruoff, *Energy Environ. Sci.*, 2012, **5**, 7936.
18 H. Wang, T. Maiyalagan and X. Wang, *ACS Catal.*, 2012, **2**, 781.
19 M. J. Ju, J. C. Kim, H.-J. Choi, I. T. Choi, S. G. Kim, K. Lim, J. Ko, I.-Y. J. Jae-Joon Lee, J.-B. Baek and H. K. Kim, *ACS Nano*, 2013, **7**, 5243.
20 X. Wang, Q. Weng, X. Liu, X. Wang, D.-M. Tang, W. Tian, C. Zhang, W. Yi, D. Liu, Y. Bando and D. Golberg, *Nano Lett.*, 2014, **14**, 1164.
21 X. Wang, X. Li, L. Zhang, Y. Yoon, P. K. Weber, H. Wang, J. Guo and H. Dai, *Science*, 2009, **324**, 768.
22 B. Guo, Q. Liu, E. Chen, H. Zhu, L. Fang and J. R. Gong, *Nano Lett.*, 2010, **10**, 4975.
23 C. Zhang, L. Fu, N. Liu, M. Liu, Y. Wang and Z. Liu, *Adv. Mater.*, 2011, **23**, 1020.
24 D. Usachov, O. Vilkov, A. Grneis, D. Haberer, A. Fedorov, V. K. Adamchuk, A. B. Preobrajenski, P. Dudin, A. Barinov, M. Oehzelt, C. Laubschat and D. V. Vyalikh, *Nano Lett.*, 2011, **11**, 5401.
25 T. Schiros, D. Nordlund, L. Plov, D. Prezzi, L. Zhao, K. S. Kim, U. Wurstbauer, C. Gutirrez, D. Delongchamp, C. Jaye, D. Fischer, H. Ogasawara, L. G. M. Pettersson, D. R. Reichman, P. Kim, M. S. Hybertsen and A. N. Pasupathy, *Nano Lett.*, 2012, **12**, 4025.
26 Y. Fujimoto and S. Saito, *Phys. Rev. B: Condens. Matter*, 2011, **84**, 245446.
27 Z. Hou, X. Wang, T. Ikeda, K. Terakura, M. Oshima and M. Kakimoto, *Phys. Rev. B: Condens. Matter*, 2013, **87**, 165401.
28 S. Wang, L. Zhang, Z. Xia, A. Roy, D. W. Chang, J.-B. Baek and L. Dai, *Angew. Chem., Int. Ed.*, 2012, **51**, 4209.
29 C. H. Choi, M. W. Chung, H. C. Kwon, S. H. Park and S. I. Woo, *J. Mater. Chem. A*, 2013, **1**, 3694.
30 J. P. Perdew, K. Burke and M. Ernzerhof, *Phys. Rev. Lett.*, 1996, **77**, 3865.
31 M. S. Josê, A. Emilio, D. G. Julian, G. Alberto, J. Javier, O. Pablo and S.-P. Daniel, *J. Phys.: Condens. Matter*, 2002, **14**, 2745.
32 N. Troullier and J. L. Martins, *Phys. Rev. B: Condens. Matter*, 1991, **43**, 1993.
33 H. J. Monkhorst and J. D. Pack, *Phys. Rev. B: Solid State*, 1976, **13**, 5188.
34 D. Ziegler, P. Gava, J. Güttinger, F. Molitor, L. Wirtz, M. Lazzeri, A. M. Saitta, A. Stemmer, F. Mauri and C. Stampfer, *Phys. Rev. B: Condens. Matter*, 2011, **83**, 235434.
35 S. Datta, *Quantum Transport: Atom to Transistor*, Cambridge University Press, 2013.
36 M. Brandbyge, J.-L. Mozos, P. Ordejn, J. Taylor and K. Stokbro, *Phys. Rev. B: Condens. Matter*, 2002, **65**, 165401.
37 Y.-H. Kim, S. S. Jang, Y. H. Jang and W. A. Goddard, *Phys. Rev. Lett.*, 2005, **94**, 156801.
38 Y.-H. Kim, J. Tahir-Kheli, P. A. Schultz and W. A. Goddard, *Phys. Rev. B: Condens. Matter*, 2006, **73**, 235419.
39 J. R. Pels, F. Kapteijn, J. A. Moulijn, Q. Zhu and K. M. Thomas, *Carbon*, 1995, **33**, 1641.
40 I. Shimoyama, G. Wu, T. Sekiguchi and Y. Baba, *Phys. Rev. B: Condens. Matter*, 2000, **62**, R6053.
41 F. Banhart, J. Kotakoski and A. V. Krasheninnikov, *ACS Nano*, 2010, **5**, 26.
42 Z. Hou, X. Wang, T. Ikeda, K. Terakura, M. Oshima, M. Kakimoto and S. Miyata, *Phys. Rev. B: Condens. Matter*, 2012, **85**, 165439.
43 R. Dronskowski and P. E. Bloechl, *J. Phys. Chem.*, 1993, **97**, 8617.
44 L. Zhao, R. He, K. T. Rim, T. Schiros, K. S. Kim, H. Zhou, C. Gutiérrez, S. P. Chockalingam, C. J. Arguello, L. Pálová, D. Nordlund, M. S. Hybertsen, D. R. Reichman, T. F. Heinz, P. Kim, A. Pinczuk, G. W. Flynn and A. N. Pasupathy, *Science*, 2011, **333**, 999.
45 T. Kondo, S. Casolo, T. Suzuki, T. Shikano, M. Sakurai, Y. Harada, M. Saito, M. Oshima, M. I. Trioni, G. F. Tantardini and J. Nakamura, *Phys. Rev. B: Condens. Matter*, 2012, **86**, 035436.
46 S. S. Kim, H. S. Kim, H. S. Kim and Y.-H. Kim, *Carbon*, DOI: 10.1039/j.carbon.2014.09.066.
47 Y.-M. Lin, A. Valdes-Garcia, S.-J. Han, D. B. Farmer, I. Meric, Y. Sun, Y. Wu, C. Dimitrakopoulos, A. Grill, P. Avouris and K. A. Jenkins, *Science*, 2011, **332**, 1294.
48 N. M. Gabor, J. C. W. Song, Q. Ma, N. L. Nair, T. Taychatanapat, K. Watanabe, T. Taniguchi, L. S. Levitov and P. Jarillo-Herrero, *Science*, 2011, **334**, 648.
49 F. Withers, T. H. Bointon, M. F. Craciun and S. Russo, *ACS Nano*, 2013, **7**, 5052.
50 F. Al-Dirini, F. M. Hossain, A. Nirmalathas and E. Skafidas, *Sci. Rep.*, 2014, **4**, 3983.
51 Y. Xue, B. Wu, H. Liu, J. Tan, W. Hua and Y. Liu, *Phys. Chem. Chem. Phys.*, 2014, **16**, 20392.
52 Y. Fujimoto and S. Saito, *J. Appl. Phys.*, 2014, **15**, 153701.